The 'zoo' of secondary instabilities precursory to stratified shear flow transition. Part 2 The influence of stratification

A. Mashayek† and W. R. Peltier

Department of Physics, University of Toronto, Ontario, M5S 1A7, Canada

The linear stability analyses described in Mashayek & Peltier (*J. Fluid Mech.*, vol. 708, 2012, 5–44, hereafter *MP1*) are extended herein in an investigation of the influence of stratification on the evolution of secondary instabilities to which an evolving Kelvin–Helmholtz (KH) wave is susceptible in an initially unstable parallel stratified shear layer. We show that over a wide range of background stratification levels, the braid shear instability has a higher probability of emerging at early stages of the flow evolution while the secondary convective instability (SCI), which occurs in the eyelids of the individual Kelvin 'cats eyes', will remain a relevant and dominant instability at high Reynolds numbers. The evolution of both modes is greatly influenced by the background stratification. Various other three-dimensional secondary instabilities are found to exist over a wide range of stratification levels. In particular, the stagnation point instability (SPI), which was discussed in detail in *MP1*, may be of great potential importance providing alternate routes for transition of an initially two-dimensional KH wave into fully developed turbulence. The energetics of the secondary instabilities revealed by our simulations are analysed in detail and the preturbulent mixing properties are studied.

Key words: shear layer turbulence, stratified turbulence, transition to turbulence

1. Introduction

In Mashayek & Peltier (2011) (hereafter referred to as *MP1*) we studied the competition between various secondary instabilities to which a primary Kelvin–Helmholtz (KH) billow, which emerges due to instability of a stratified parallel shear flow, is susceptible. We focused primarily upon two instabilities, namely the secondary convective instability (SCI) (Klaassen & Peltier 1985) and the secondary shear instability (SSI) (Corcos & Sherman 1976). The SCI is induced by the emergence of convectively unstable regions in the billow cores during the roll-up of a train of KH waves. In *MP1* we presented a heuristic model which predicted the dependence of the Rayleigh number of the core unstable regions (Ra^u) on the Prandtl number, Pr, the Reynolds number, Re, and the gradient Richardson number at the midpoint of the initially parallel shear layer, Ri_0. Susceptibility maps were provided which identified regions in Re–Pr–Ri_0 parameter space where the SCI is

most probable. The non-dimensional control parameters Re, Pr and Ri_0 are defined as

$$Re = \frac{U_0 h}{\nu}, \quad Pr = \frac{\nu}{\kappa}, \quad Ri_0 = \frac{N^2}{(\mathrm{d}\bar{U}^*/\mathrm{d}z^*)^2}, \quad (1.1)$$

where U_0 is the reference velocity assumed to be equal to half the velocity difference across the shear layer, h is half of the shear layer thickness, ν is the kinematic viscosity, κ is the thermal diffusivity, N is the buoyancy frequency, $\bar{U}^*$ is the height-dependent dimensional velocity in the shear layer, and z^* is the dimensional vertical co-ordinate measured from the centre of the shear layer.

To study the relative importance (in terms of growth rate) of SSI and SCI, in *MP1* we performed non-separable secondary stability analysis (of Klaassen & Peltier (1985) type) on one specific case which was chosen (based on the predictions of the heuristic model) to be in a region in the Re–Ri_0 parameter space which lies between the region in which SSI is not expected to appear and the region in which this instability is expected to be realized. In this method the flow is assumed to be periodic in the streamwise direction and is decomposed into a quasisteady, two-dimensional component which represents the primary KH wave and a small-amplitude three-dimensional component of the form $\boldsymbol{u}_{3D}(x, y, z, t) = \boldsymbol{u}_0(x, z) \exp[\mathrm{i}dy + \sigma t]$ (with a similar form for the density field) where $\boldsymbol{u}_0$ corresponds to the velocity of the background KH wave and d and σ are the spanwise wavenumber and growth rate of the three-dimensional perturbations. The results described in *MP1* demonstrated that the SSI mode has an excellent chance of growing at an early stage of flow evolution when the braid length is maximum and before it comes to be suppressed by the growth of the cores. It was also shown that throughout the life-cycle of the KH wave the SCI mode had a high probability of emerging. The analyses also revealed the existence of two other three-dimensional secondary instabilities, namely the stagnation point instability (SPI) and the secondary vorticity band instability (SVBI). Finite-amplitude growth of either of these two instabilities could conceivably eliminate or trigger the onset of SSI by inducing braid deformation.

In this paper we pursue two main goals. First, we further evaluate the predictions of the heuristic model which describes the dependence of emergence of SCI and SSI on Re and Ri_0 by extending the range of our stability analyses; second, we study the energetics of the secondary instabilities we have found and explore their contributions to the early phase of evolution of a KH wave, a phase which is associated with efficient mixing. Our main goal is to investigate the relative influence of stratification on the four main modes of instability introduced in *MP1* (namely the SCI, SSI, SPI and SVBI modes). The cases which we will consider in this study are listed in table 1. The governing equations, domain size, numerical techniques and diagnostic tools to be employed are identical to those of *MP1*. Case c1-1000-0.12 was considered in detail in *MP1* and we will frequently refer to it for comparison purposes. Hereafter, when referring to figures and equations from *MP1*, we will use the suffix '-*MP1*' (e.g. figure 1-*MP1* means figure 1 from *MP1*).

In the final section of this paper we analyse the energetics of the secondary instabilities and their contributions to the preturbulent phase of mixing in an evolving KH wave. It has been shown (Caulfield & Peltier 2000; Smyth & Moum 2000; Staquet 2000; Smyth 2003 or see Peltier & Caulfield 2003 for a review) that the preturbulent mixing in KH waves is highly efficient and extends over a considerable period of time of the life cycle of a KH wave. Therefore, preturbulent mixing contributes significantly to the overall mixing and is worthy of being studied in detail to partially address

Case name	Grid ($Nx \times Nz$)
$c1\text{-}1000\text{-}0.12$	768×800
$c1\text{-}2000\text{-}0.04$	768×800
$c1\text{-}2000\text{-}0.12$	768×800
$c1\text{-}2000\text{-}0.16$	768×800
$c1\text{-}2000\text{-}0.20$	768×800

TABLE 1. Two-dimensional numerical simulations performed for providing the time evolution of the background flow, needed by the secondary stability analysis. Similar to *MP1*, the flow domain is 30*h* in the vertical direction and 28.56*h* in the streamwise direction. Also similar to *MP1*, cases are named in the *cPr–Re–Ri*$_0$ format.
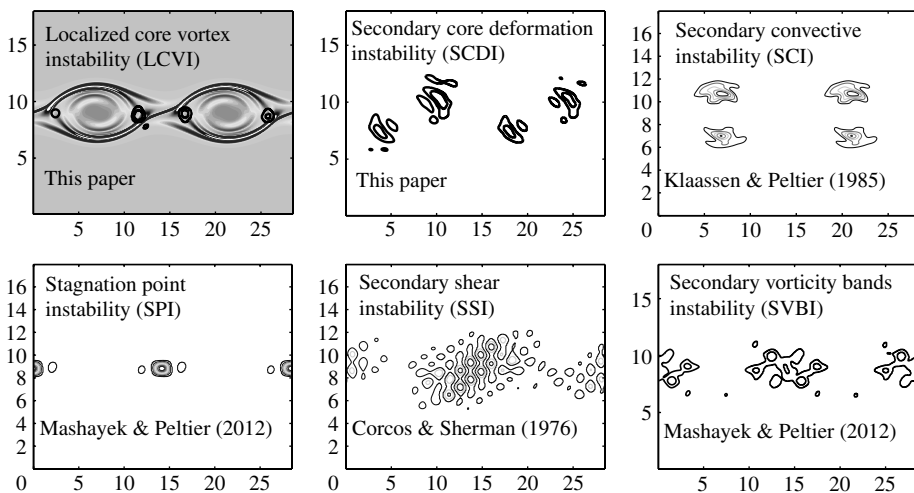

FIGURE 1. Lexicon of various secondary instabilities discussed in *MP1* and in this paper. Each frame contains the reference to the original study which provides details of its corresponding instability. The horizontal and vertical axes correspond to *x* and *z* coordinates, respectively. The underlying background KH wave is shown in the first panel to provide the reference of the KH wave basic state in terms of which the location of each instability is illustrated in the other frames of the figure.

the variations in mixing efficiency reported in observational studies (Gargett & Moum 1995; Moum 1996; Ruddick, Walsh & Oakey 1997; Smyth, Moum & Caldwell 2001). Our method of quantifying the mixing will be similar to that of Caulfield & Peltier (2000) which is an extension of that due to Winters *et al.* (1995) which itself was built upon the work of Lorenz (1955).

We repeatedly refer to several secondary instabilities in this paper by referring to their acronyms. The secondary instability lexicon of figure 1 is provided as a reference to which the reader may refer if needed. References to the literature will appear in italics (e.g. *MP1*) while the acronyms we employ for the suite of secondary instabilities whose spatial locations within the background wave are illustrated in figure 1 will not be italicized.
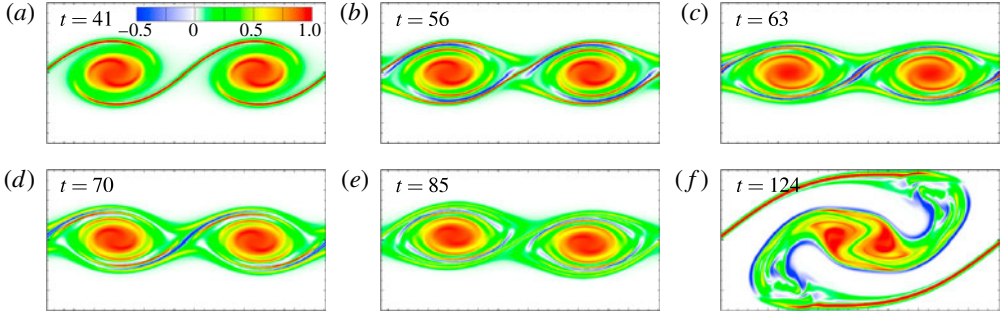
FIGURE 2. Spanwise vorticity contours at various stages of flow evolution for c1-2000-0.04.

2. Stability analysis for the case c1-2000-0.04

As the first case of interest beyond the single case discussed in *MP1* we consider c1-2000-0.04. Figure 2 shows the evolution of the vorticity field of the flow for a sequence of times in the course of its evolution. Compared with c1-1000-0.12 (discussed in *MP1*), this case has a higher Reynolds number and a lower Richardson number. The figures reveal no trace of SSI, or of any other mechanism of secondary vortex formation on the braid. By $t = 56$, the negative vorticity bands in the cores have grown sufficiently intense and come sufficiently close to the stagnation point to cause a slight deformation at the centre of the braid. At $t \sim 65$, the braid's vorticity is exhausted and by $t = 70$ a braid with vorticity of opposite sign has formed. This transition marks the onset of the pairing process. Beyond this point, the pairing instability grows and a strong braid with positive vorticity is re-established. As figure 2(f) shows, no sign of SSI is observed even on the postmerging braid. This is in agreement with the predictions of the heuristic analysis of *MP1* for $Re = 2000$ and $Ri_0 = 0.04$.

Figure 3 provides a range of flow diagnostics for this case. Figure 3(a) shows the evolution of the kinetic energy of the KH wave, $\mathcal{K}_{KH}$. The local peak of the curve at $t = 41$ identifies the climax time (denoted by t^*) which is the time at which the background KH wave achieves its maximum kinetic energy. The second episode of increase in this time series corresponds to growth of the vortex pairing instability. Figure 3(b) shows the plot of δ_{pair}, which represents the horizontal distance between the tips of the most intense blue vorticity bands inside the cores, a time series which demonstrates that at $t \sim 65$ the vorticity bands meet and merging begins. This is verified in the plot of Δz_{cores} in figure 3(c) which denotes the differential vertical deflection of the cores. Figure 3(d) illustrates the evolution of the braid normal Richardson number at the stagnation point. Even though Ri_B^{Stag} does diminish well below the value of 0.25, it rapidly recovers thereafter to large values. The Richardson number drops to a near-zero value at $t \sim 65$ due to the draining of vorticity from the braid. By that time too little remains of the braid to accommodate the SSI. As for the SPI, figure 5-*MP1* shows that this case has too large a value of γ_s/Ω (where γ_s is the strain rate at the stagnation point and Ω is the braid vorticity) for the SPI to grow. Figure 3(e) shows the time variations of the growth rates for the fastest growing modes (FGMs) of various secondary instabilities. Comparing the curves for SCI (at $d = 8$) and SSI (at $d = 0$) shows that at early stages of flow evolution (prior to t^* depicted approximately by the vertical dashed line in the figure), the SSI has a growth rate comparable to or even larger than that of the SCI. However, SSI weakens with time
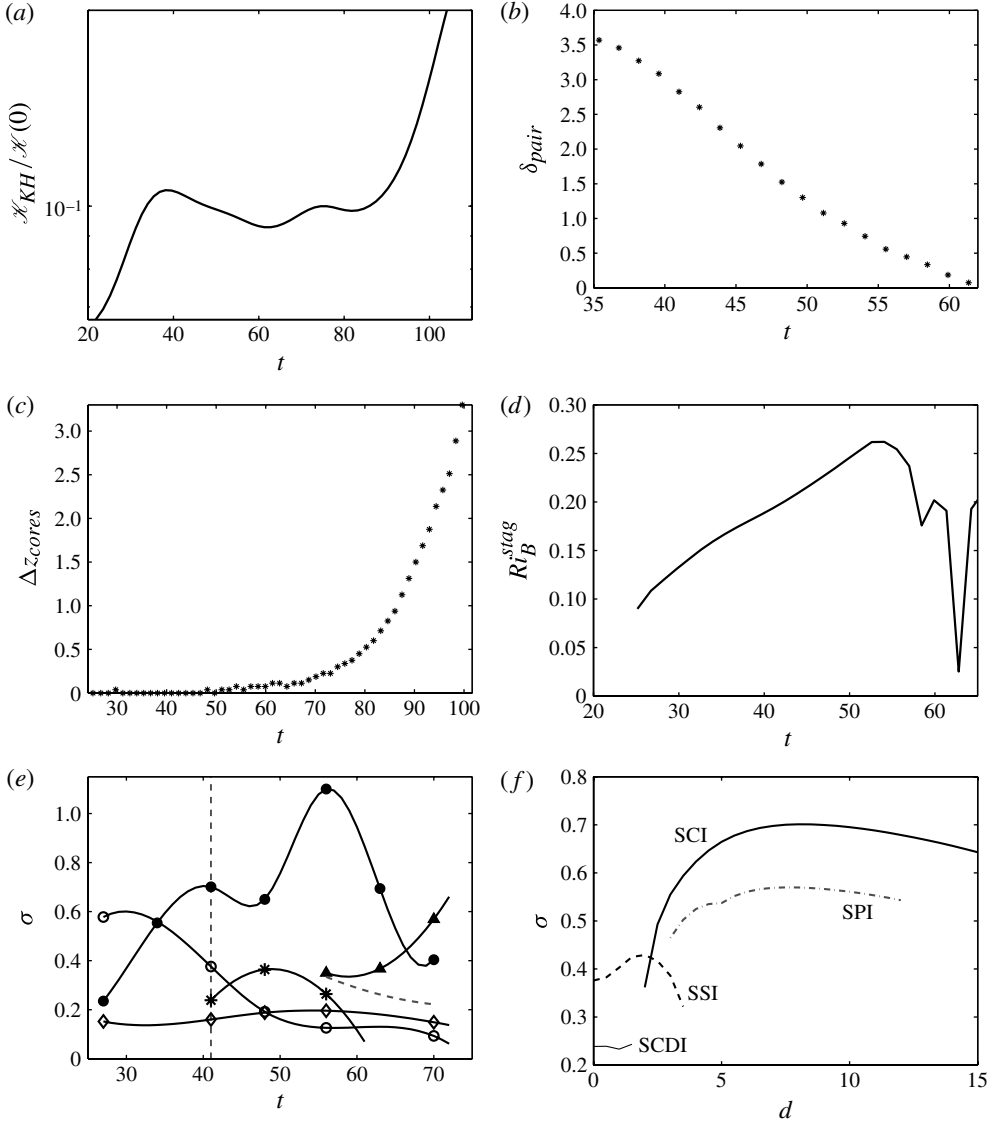
FIGURE 3. Results for case $c1$-2000-0.04: (*a*) kinetic energy of the nonlinear KH wave, $\mathcal{K}_{KH}$, normalized by $\mathcal{K}(0)$; (*b*) δ_{pair}; (*c*) Δz_{cores}; (*d*) Ri_B^{stag}; (*e*) results of the stability analysis for the FGM of various modes during the flow evolution; and (*f*) growth rate versus the spanwise wavenumber, d, for various modes. Line attributes in (*e*) are: solid line with filled circles for SCI at $d = 8$; solid line with hollow circles for SSI at $d = 0$; solid line with hollow diamonds for the pairing instability at $d = 0$; solid line with stars for SCDI at $d = 0$; solid line with filled triangles for SPI at $d = 7$; and thick dashed line for SVBI at $d = 0$. The vertical thin dashed line shows the climax time, t^*.

due to the strain field associated with the vortex cores while SCI strengthens. For most of the duration of flow evolution, the three-dimensional SCI modes remain dominant (in terms of growth rate). Comparing the SSI curve in figure 3(*e*) with the Ri_B^{stag} curve
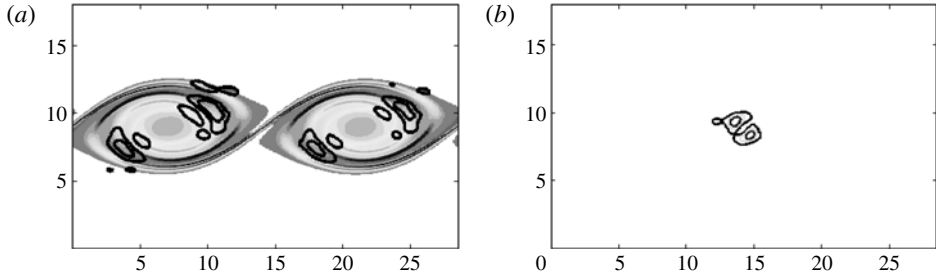
FIGURE 4. (*a*) The density eigenfunction for the fastest growing SCDI mode ($d = 0$) at $t = 41$ overlaid on the vorticity contours; (*b*) the $\mathcal{K}'$ eigenfunction for the FGM of the three-dimensional SPI sequence ($d = 7$) at $t = 70$.

in figure 3(*d*) shows that as the braid stagnation point Richardson number increases rapidly between $t = 30$ and $t = 50$, the growth rate of SSI decreases dramatically.

Other growth rate curves in figure 3(*e*) include that for the pairing mode, which has a small growth rate compared with the other instabilities but is long lived, the SVBI mode which appears only for a limited range of time, the SPI mode which comes into play at later stages of the flow evolution and a further new instability which was not revealed in the lower-Reynolds-number analyses of *MP1* and which we will refer to here as the secondary core deformation instability (SCDI). The density eigenfunction of this mode for time t^* is shown in figure 4(*a*) which reveals the tendency of this mode to inflate the vortex cores. As shown in figure 3(*e*), this mode has significant growth rate only for a limited range of time. This mode is oscillatory (i.e. it has a non-zero σ_i) and extracts most of its energy from the strain field of the background flow (i.e. $\mathcal{S}t$ in equation (4.13-*MP1*)).

Figure 4(*b*) shows the $\mathcal{K}'$ eigenfunction for the FGM of three-dimensional SPI ($d = 7$) at $t = 70$. Among the various modes considered in figure 3(*e*), only the pairing, SSI, SVBI and SCDI modes would be expected to have any chance of emerging in two-dimensional simulations. Since the growth rate of SSI and SCDI decreases with time as $t \rightarrow 65$, they do not emerge in our simulation and thus only the pairing instability is fully realized. In the time window $55 < t < 70$ however, the SVBI does lead to the development of a slight braid deformation as shown in figure 2.

Figure 3(*f*) shows the variations in the growth rate of various modes versus the spanwise wavenumber. All curves are plotted for t^* except for the SPI curve which is plotted for $t = 70$ (SPI is not yet detected at t^*). The fastest growing SCI mode has a spanwise wavenumber of $d = 8$ whereas the SPI peaks at $d = 7$ and the SSI peaks at $d = 2$. The SCDI mode is also of a three-dimensional nature but its FGM is two-dimensional and there is a cut-off wavenumber of $d \sim 2$. In the time range $t = 40$–55, the first few dominant eigenvalues for small 'd' correspond to the SCDI.

3. Stability analysis for the case $c1$-2000-0.12

We turn our attention next to case $c1$-2000-0.12. The flow visualizations for the background flow are presented in figure 5. Once the intense vorticity bands of the core extend so as to become sufficiently close to the braid, an instability which leads to deformation of the braid and roll-up of two small secondary vortices occurs. Once the cores' vorticity bands reach the braid, the braid vorticity is drained ($90 < t < 100$) and this marks the onset of pairing. The postpairing braid is prone to SSI as it satisfies
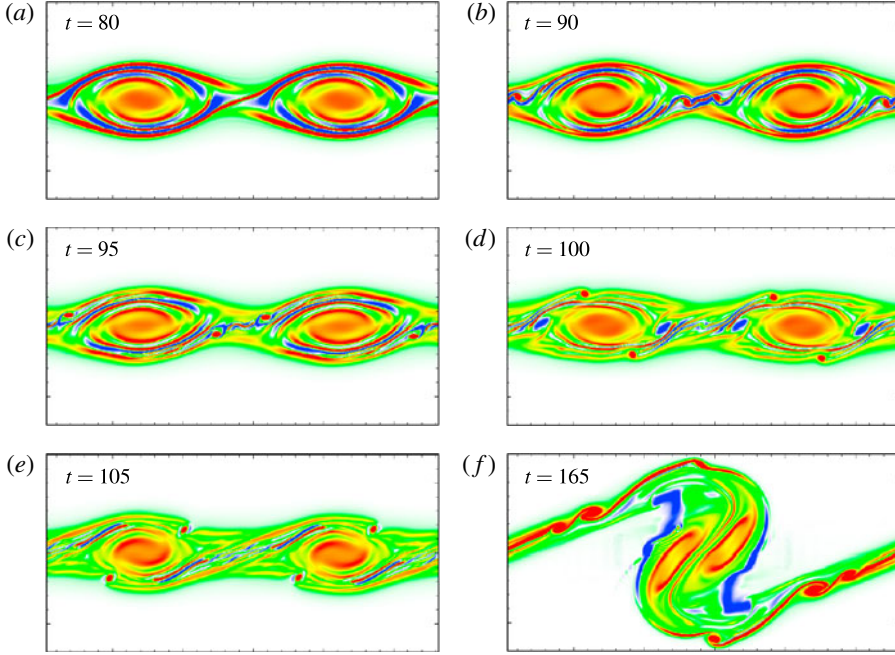
FIGURE 5. Spanwise vorticity contours at various stages of flow evolution for $c1$-2000-0.12.

the Ri_B and γ/Ω conditions required for SSI to grow as discussed in *MP1*. Even though the prepairing braid has almost the same Ri_B value, the suppressing influence of the strain field inhibits growth of SSI vortices.

Figure 6 presents plots similar to figure 3 for this case. Figure 6(*a*) shows that the background KH wave obtains its maximum kinetic energy at $t^* = 59$. The second rise in $\mathscr{K}_{KH}$ beyond $t = 100$ corresponds to the pairing process. Figure 6(*b,c*) show that the onset of the pairing instability coincides with the same time that the cores' blue vorticity bands meet at the braid. Figure 6(*d*) shows that Ri_B^{stag} decreases almost uniformly from a value of ~ 0.2 at t^* up to the point when it falls sharply to zero at $t \sim 85$ (due to braid vorticity draining). This time is coincident with the $\delta_{pair} = 0$ point in figure 6(*b*) and the onset of $\Delta z_{cores} > 0$ in figure 6(*c*). Figure 6(*e*) shows the results of the secondary stability analysis for this case. Similar to previous cases, SCI still obtains the highest growth rate over a wide range of time. However, for a considerable time period in the early stages ($40 < t < 65$), the SSI has a growth rate comparable to the SCI. Here σ_{SSI} grows slightly in the time range $40 < t < 65$ which is the same time as the decline in Ri_B^{stag} occurs (figure 6*d*). Therefore, SSI has a high chance of emerging at an early stage of flow evolution while its chances rapidly diminish because of the growing strain field induced by the vortex cores. Nevertheless, the two-dimensional simulation which has provided the background flow for the stability analysis of this case does not show emergence of SSI. The secondary vortices formed on the braid in figure 5 are actually due to the SVBI.

Among the additional instabilities tracked in figure 6(*e*) is the SCDI which has a growth rate smaller than the SSI but larger than the pairing instability. All three of these instabilities are characterized by slight variations in their growth rates with time. Similar to the previous case, the growth rate of the SPI (for $d > \sim 8$) becomes
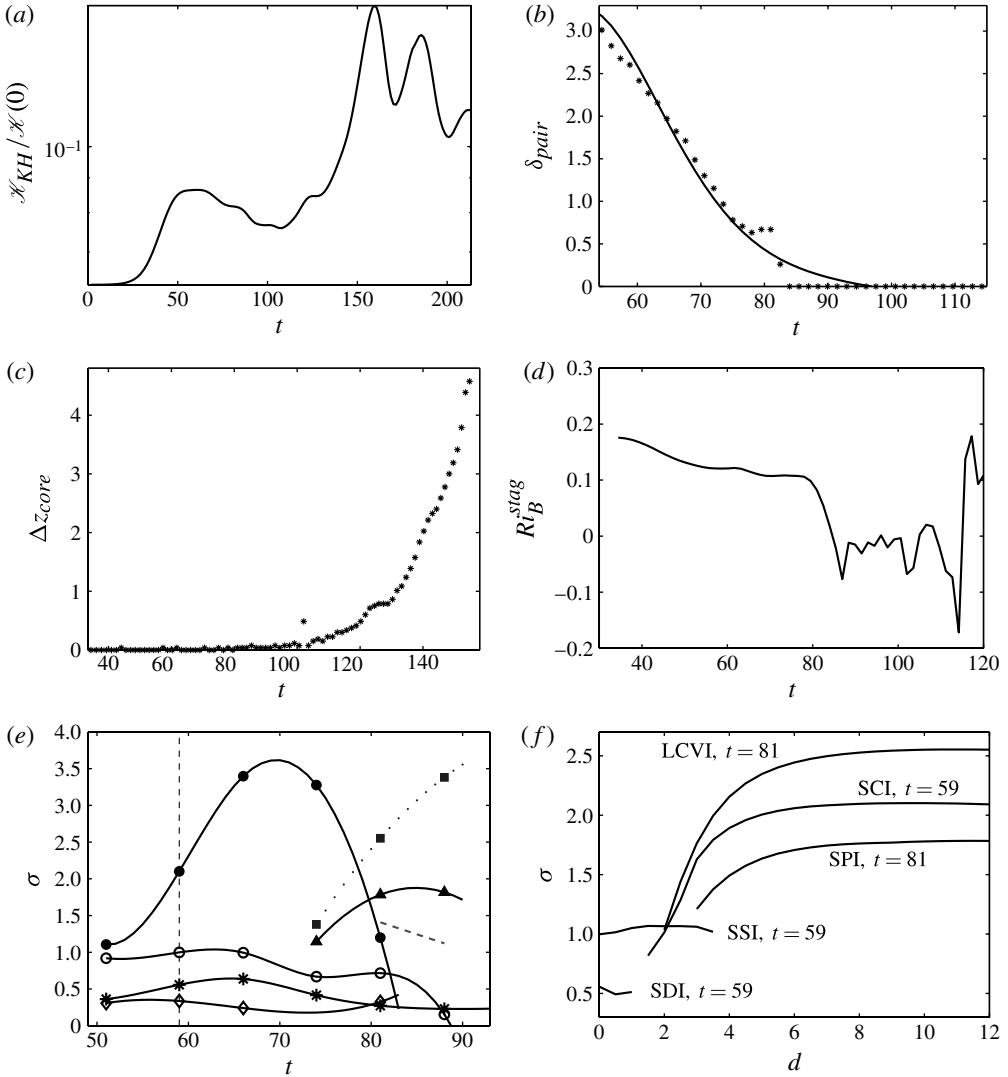
FIGURE 6. Same as figure 3 but for $c1$-2000-0.12. Line attributes in (e) are: solid line with filled circles for SCI at $d = 10$; solid line with hollow circles for SSI at $d = 0$; solid line with hollow diamonds for the pairing instability at $d = 0$; solid line with stars for SCDI at $d = 0$; solid line with filled triangles for SPI at $d = 11.5$; the dashed line for SVBI at $d = 0$; and the dotted line with filled squares for LCVI at $d = 11$.

significant at later stages of flow evolution. Our analysis detects this mode for times beyond $t = 70$. Another three-dimensional instability is detected for this case and its saturated growth rate for $d > \sim 8$ is shown in figure 6(e) as a dotted line with filled squares. This mode has a continuous spectrum of spanwise wavenumbers ranging from very small 'd' (near zero) to very large values ($d = 12$ was the upper limit to which our analyses were extended). Figure 7 shows the eigenfunctions of this instability for $d = 2$ (figure 7a) and $d = 10$ (figure 7b). This instability implies the tendency of formation of counterclockwise vortices at the tips of the blue (negative) vorticity bands
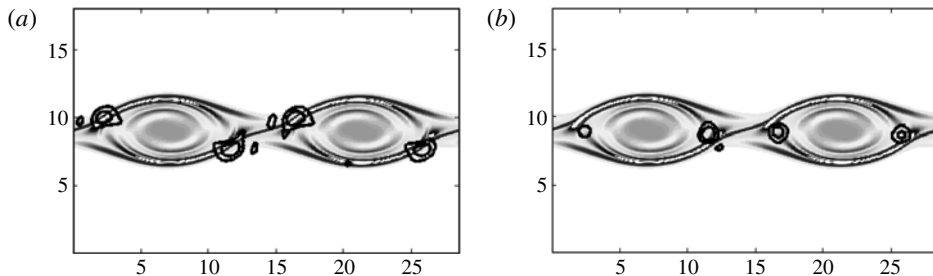
FIGURE 7. The density eigenfunction for the fastest growing LCVI mode at $t = 81$: (*a*) $d = 0$ and (*b*) $d = 10$.

in the cores. Therefore, we refer to this instability as a localized core vortex instability (LCVI). Once the vorticity bands have grown large enough in the cores, the LCVI can emerge provided that the vorticity magnitude is also strong enough inside the band. The strength of the vorticity bands increases with the stratification (Ri_0). That is why this instability was not detected for the case $c1$-2000-0.04. Moreover, a higher Reynolds number also promotes LCVI since it makes the roll-up process faster leaving less time for the vorticity gradients inside the cores to diffuse. This explains why this mode was not detected for case $c1$-1000-0.12. A close look at figure 5 shows that apart from the positive-vorticity vortices formed on the braid (red vortices), negative (blue) vortices also form inside the cores which establish the emergence of the LCVI.

Figure 6(*f*) plots the variations in the growth rates versus the spanwise wavenumber for various modes detected for this case. The curves in the plot are made at the KH wave climax state for SSI, SCI and SDI and at $t = 81$ for the late emerging instabilities, SPI and LCVI. Although the σ_{SSI} shows small variations with d, the SSI curve extends to larger values of d compared with the case $c1$-1000-0.12. This implies that the scales of motion associated with SSI have become smaller with increase in the Reynolds number. Figure 6(*f*) shows that the growth rates of SPI, SCI and LCVI all saturate for $d > 8$ indicating that there will be no preferred wavelength for the instabilities and that the flow is capable of injecting energy into very small scales of the motion, facilitating a rapid and direct transition to turbulence.

We should point out that the eigenfunction for the SVBI shown in figure 10-*MP1* appears to be a combination of LCVI and SPI at $d = 0$. There is the possibility that SVBI is just the long-wave manifestation of these two modes. It should be noted that detection of the short-wave instabilities (such as the SPI, LCVI and SCI) by our stability analysis becomes difficult as $d \to 0$ because such long-wave modes (such as SSI, pairing and SDI) all dominate the eigenvalue hierarchy for small 'd'. However, once d is set to be exactly zero rather than close to zero, a large number of long-wave but three-dimensional modes are automatically eliminated allowing for two-dimensional version of SPI to emerge in the analysis. Nevertheless, since the eigenfunction shown in figure 10-*MP1* seems to be effective both in the middle of the braid and on vorticity bands inside the cores, we choose to keep treating it as an independent instability.

4. Flow analysis for the case $c1$-**2000-0.16**

The flow conditions for this case are close to those of the case ($c1$-2000-0.12) and so we do not present the results from the stability analysis for this case.

Figure 8 shows a sequence of flow visualizations from the simulation of the two-dimensional background flow for this case. At time $t = 100$, the corners of the blue vorticity bands have expanded sufficiently and are strong enough that a counterclockwise vortex forms in each of these regions. This can be seen in the enlarged version of the graph overlaid with streamlines for time $t = 110$. The formation of these vortices is due to the finite-amplitude growth of the LCVI modes described in figure 7. It is important to remember that this mode is of a three-dimensional nature and its FGM a spanwise wavenumber $d > 10$. Hence, the evolution of these vortices in our two-dimensional simulation are expected to be significantly different in a three-dimensional simulation. The presence of these vortices in the blue vorticity bands leads to a slight deformation of the braid which is just sufficient to induce formation of secondary shear vortices on the braid. This is seen in the figure for $t = 105$. The braid deformation induced by the LCVI continues exciting generations of multiple secondary vortices on the braid as the flow evolves up to $t = 116$. The location of generation of the braid vortices remains quasi-steady up to $t = 110$ and, hence, the streamlines and the vorticity fields are aligned. For the pair of vortices which have already moved to the periphery of the cores at $t = 110$, however, the instantaneous streamlines do not follow the vorticity pattern as the vortices are moving rapidly with respect to the cores. These vortices move along the periphery of the cores, deform the vorticity layers and lead to enhanced mixing inside the cores. In the meantime, the vortices formed at the corner of the large blue vorticity bands (due to LCVI) diffuse. The vorticity contour at $t \sim 110$ establishes the emergence of the SVBI in the flow (which again can be interpreted as a combination of the SPI and LCVI in the $d \rightarrow 0$ limit).

5. Stability analysis for the case $c1$-2000-0.2

As the last case to which we will apply our methodology for secondary stability analysis, we consider $c1$-2000-0.2. The vorticity contours at different stages of the flow evolution for this case are plotted in figure 9. Owing to the very high level of stratification, the maximum amplitude of the KH wave is small compared with the previous cases we have considered. The corresponding t^* for this case is $t = 116$. As the flow visualizations demonstrate, no significant modification of the flow field by secondary instabilities occurs. At a time near $t \sim 175$ the braid vorticity draining event occurs and the onset of the pairing instability is marked. Although it is not clearly observed in the last panel of the figure, the pairing instability is well underway at $t = 259$ and a new positive vorticity braid has formed once more. The growth rate of the pairing instability is very weak, however, due to the suppressing influence of the stratification. As shown in the figure, for $t > 150$, the upper and lower positive (red) vorticity bands which mark the outer limits of the two cores almost connect allowing for an alternate way of transporting vorticity between the cores. Although this was also observed for the $c1$-2000-0.12 and $c1$-2000-0.16 cases, the connection seems to be stronger for this case.

Figure 10 shows the results of the stability analysis for this case. Since most secondary instabilities seem to be suppressed by the stratification (based on the two-dimensional simulation of the background flow), we focus on four main instabilities namely SCI, SPI, SSI and pairing. Comparing the curves for σ_{SCI} and σ_{SSI} shows that the SCI is still the dominant instability (in terms of growth rate) by far. Comparing the SSI curve with that of the previous case ($c1$-2000-0.12) shows that because of the suppressing influence (due to both the evolution of the strain field and shortening of
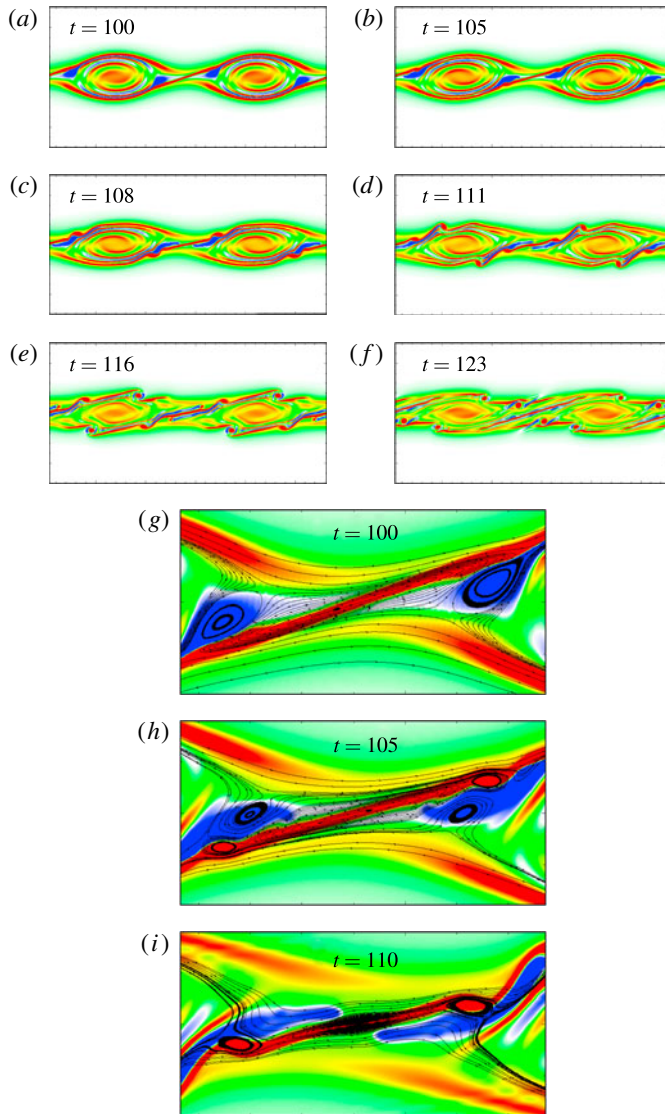
FIGURE 8. Vorticity contours at various stages of flow evolution of case $c1$-2000-0.16. Streamlines are superposed on an enlarged view of the braid in $(g–i)$. The colourbar is the same as figure 2.

the braid as a result of the growth of the cores) of the growth of the cores on the braid, the SSI is enhanced with increase in the stratification. Based on figure 10 we conclude that SCI and SPI will most probably break down this flow into turbulence in a three-dimensional case with the possibility of LCVI playing an important role.

Apart from the major instabilities discussed in figure 10, a continuous spectrum of LCVI modes was also detected for $d \geqslant 0$ for times beyond t^*. Similar to case $c1$-2000-0.12, the growth rates of LCVI, SCI and SPI all saturate for $d > 8$.

Figure 9(a) shows that locations where the strongest negative (blue) vorticity bands in the two cores meet the braid (at $t = 132$) are separated by some distance in contrast
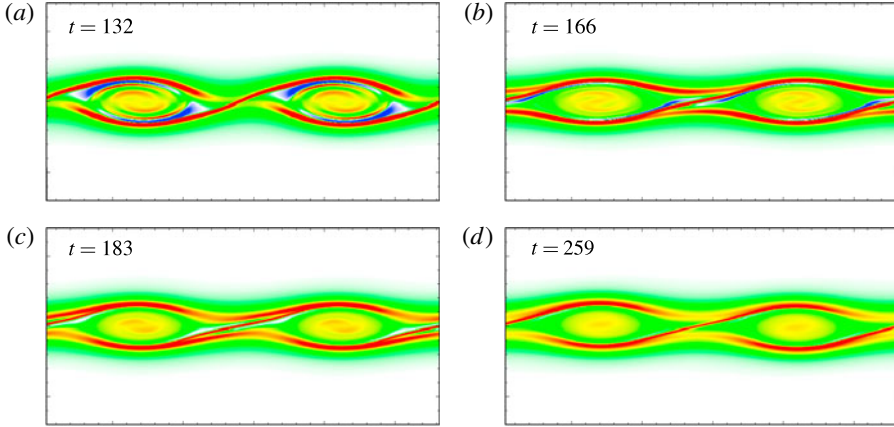
FIGURE 9. Vorticity contours at various stages of flow evolution for $c1$-2000-0.2.
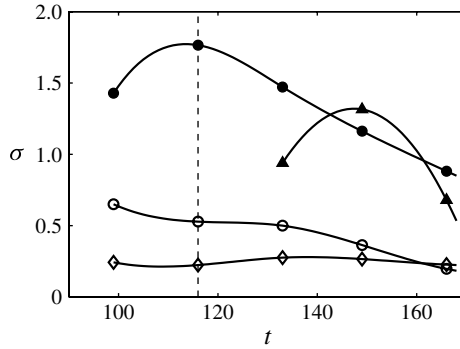

FIGURE 10. Growth rate of various instability modes obtained from the stability analysis for case $c1$-2000-0.2: solid line with filled circles for SCI at $d = 9$; solid line with hollow circles for SSI at $d = 0$; solid line with hollow diamonds for the pairing instability at $d = 0$; and solid line with filled triangles for SPI at $d = 10$. The vertical thin dashed line corresponds to t^*.

to previous cases where the two locations coincided at the stagnation point. Therefore, the eigenfunctions corresponding to the SPI are considerably different from those of previous cases. To show this, we plot the eigenfunctions for the FGM of the SPI for $d = 10$ at $t = 149$ in figure 11(a) and for the $d = 0$ mode at $t = 166$ in figure 11(b). Both panels show the tendency of the cores' vorticity bands to deform the braid at two locations. The distance between the two locations decreases with time leading to their ultimate merging at the stagnation point (LCVI to SPI transition). It should also be noted that SCDI is not detected for this case implying the possibility of total suppression of it due to enhanced stratification and the smaller sizes (associated with high Ri_0) of the vortex cores.

6. A summary of the effects of stratification upon the mechanisms of turbulent collapse

To summarize the influence of stratification on the dominant secondary instabilities that could play significant roles in the transition to fully developed turbulence,
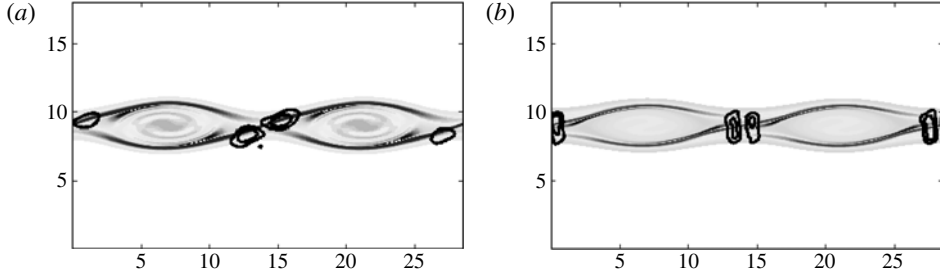
FIGURE 11. Vorticity contours of the case $c1$-2000-0.2 overlaid with density eigenfunctions of the (a) fastest growing $d = 10$ SPI mode at $t = 149$ and (b) fastest growing $d = 0$ SPI mode at $t = 166$.

figure 12 plots the growth rates for SCI, SSI, SPI and pairing instabilities for the three cases considered in this study plus the additional case considered in *MP1*. To allow for direct comparison between this sequence of cases, the zero of time is centred on the instant at which the background KH wave achieves its maximum kinetic energy (the climax state) for each case. For the corresponding spanwise wavenumbers of the SCI and SPI modes shown in the figure, see figures 3, 6 and 10 from this article and figure 17-*MP1*. The SSI and pairing modes are for $d = 0$ as their FGMs are nearly two dimensional (see *MP1* for a discussion).

Figure 12(a) compares σ_{SCI} for the four cases. All curves are characterized by an increasing–decreasing pattern in agreement with the evolution of the Rayleigh number of statically unstable regions, Ra^u, inside the cores (*MP1*). Comparing the three $Re = 2000$ cases, the SCI becomes stronger as the Richardson number is increased from 0.04 to 0.12 due to increased density difference across the core unstable regions, $\Delta\rho^u$, at higher Ri_0 (remembering that $Ra^u \propto \Delta\rho^u$). As Ri_0 is increased from moderate values (0.12) to very high values (0.2), however, σ_{SCI} is suppressed considerably due to the decrease in the rate of evolution of the primary KH wave. This increase in the characteristic time scale allows for increased diffusion of the density difference across the core unstable regions hence diminishing the tendency for overturning. Moreover, at high Ri_0, the thickness of the unstable region is sharply reduced due to smaller amplitude of the KH billows. This further contributes to a smaller Ra^u ($Ra^u \propto \delta_\rho^{u^3}$). Comparing the curve for cases $c1$-1000-0.12 and $c1$-2000-0.12 shows that an increase in the Reynolds number leads to an increase in the σ_{SCI} as predicted by the heuristic model in *MP1*. Figure 12(b) compares σ_{SSI} for all four cases. At early stages of the KH wave evolution σ_{SSI} is largest and it diminishes with time due to the core-induced flow field surrounding the braid. Therefore, secondary shear vortices have a much greater chance of emerging at early stages of the KH roll up for a wide range of stratification levels. Comparing the three $Re = 2000$ cases, similar to the SCI, σ_{SSI} grows larger from $Ri_0 = 0.04$ to $Ri_0 = 0.12$ and decreases from $Ri_0 = 0.12$ to $Ri_0 = 0.2$. As the braid Richardson number, Ri_B, is inversely proportional to Ri_0, an increase in Ri_0 from 0.04 to 0.12 leads to a smaller Ri_B promoting the chances of occurrence of SSI. As Ri_0 tends from 0.12 to 0.2 however, the suppressing influence of the flow field induced by the growing cores increases leading to a smaller growth rate. Comparing the curve for cases $c1$-1000-0.12 and $c1$-2000-0.12 shows that an increase in the Reynolds number enhances the probability of SSI as expected based on the heuristic model of *MP1*.
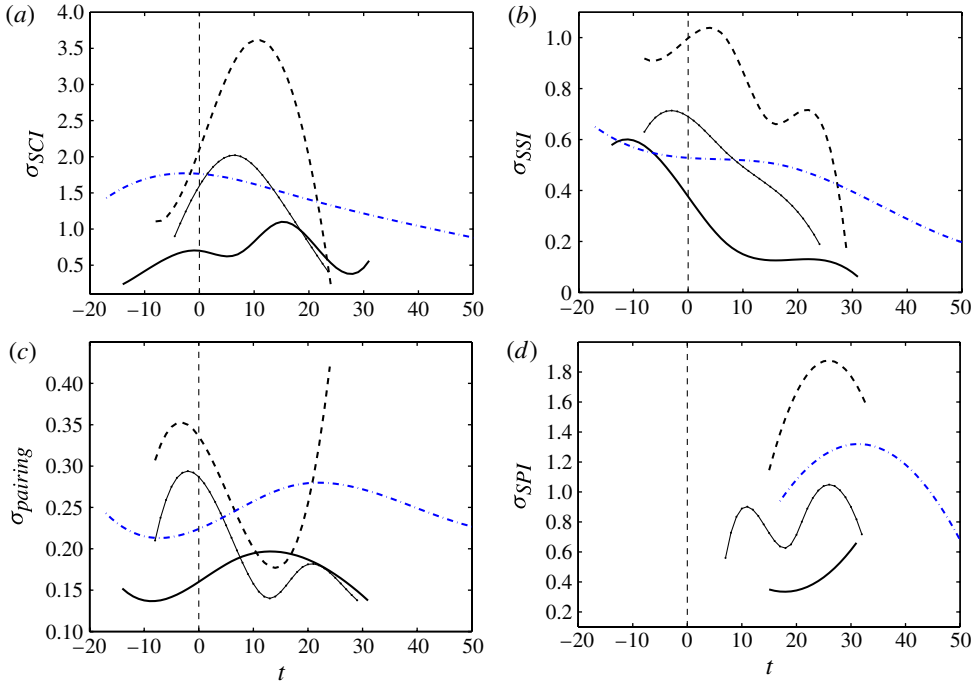
FIGURE 12. (Colour online) Comparison between the growth rates of various instabilities for the three cases considered by the stability analysis in this study plus the one case considered in *MP1*. Growth rates are for: (*a*) SCI; (*b*) SSI; (*c*) pairing instability; and (*d*) SPI. The line attributes in each panel are: thick solid line for case $c1$-2000-0.04; dashed line for case $c1$-2000-0.12; dash–dotted line for case $c1$-2000-0.2; and thin solid line (overlain by dots) for case $c1$-1000-0.12 from *MP1*. Each curve is shifted by its corresponding t^* so then all curves start from the instant of maximum $\mathcal{K}_{KH}$.

Figure 12(*c*) compares $\sigma_{pairing}$ for all four cases. Comparing the range of the vertical axis in this panel with the other three panels shows that the growth rate of the pairing instability does not vary much for moderate to high values of Ri_0 and from $Re = 1000$ to $Re = 2000$. The sensitivity to the Reynolds number in particular seems to be very weak. The variation in $\sigma_{pairing}$ follows the same trend as the other instabilities in figure 12: increase from small stratification to moderate stratification, and decrease from moderate to high stratification.

Figure 12(*d*) shows that σ_{SPI} becomes highly significant at later stages of flow evolution and once the cores' vorticity bands become sufficiently close to the stagnation point to induce the perturbation necessary for the onset of SPI. The growth rate of the SPI, according to the results of our analyses is very sensitive to both Ri_0 and Re. Here σ_{SPI} also increases from $Ri_0 = 0.04$ to $Ri_0 = 0.12$ and decreases from $Ri_0 = 0.12$ to $Ri_0 = 0.2$. Comparing the $c1$-1000-0.12 and $c1$-2000-0.12 curves shows that an increase in the Reynolds number leads to a considerable increase in σ_{SPI}.

In general, figure 12 shows that $\sigma_{SCI} > \sigma_{SPI} > \sigma_{SSI} > \sigma_{pairing}$. This hierarchy should not be taken to imply which instability should dominate because the spatial locations and the time ranges over which the instabilities persist do not necessarily overlap and their growth rates do not remain constant over time. Moreover, onset of one instability may trigger or inhibit emergence of another. According to the figure, increase in the

Reynolds number enhances the growth rates of all secondary instabilities as well as the spanwise wavenumber of the FGM.

7. Energetics of secondary instabilities and their contributions to preturbulent mixing

It has been demonstrated previously that the mixing efficiency is high (close to unity) during the period of time prior to onset of fully developed turbulence (Winters *et al.* 1995; Caulfield & Peltier 2000; Smyth *et al.* 2001, as reviewed in Peltier & Caulfield 2003). This is a consequence of the small dissipation rate during this phase of flow evolution. Since the preturbulent phase occupies a significant portion of the total life cycle of a KH wave, when the initial conditions include only weak noise, we intend in this section to quantify the contributions of the newly discovered instabilities which can exist in the laminar phase of the flow to the preturbulent mixing. We also investigate the reservoirs from which secondary instabilities extract their energies. To examine the influence of the braid instabilities on the mixing process, we compare cases with no significant braid activity (cases $c1$-1000-0.12, $c1$-2000-0.04 and $c1$-2000-0.2) with cases with braid deformation and vortex formation on the braid ($c1$-2000-0.12 and $c1$-2000-0.16).

Following Caulfield & Peltier (2000), the time rate of change of the total mechanical energy of the system under consideration, E, can be written as

$$\frac{\mathrm{d}E}{\mathrm{d}t} = \frac{\mathrm{d}\mathscr{K}}{\mathrm{d}t} + \frac{\mathrm{d}\mathscr{P}}{\mathrm{d}t}, \tag{7.1}$$

where $\mathscr{K}$ and $\mathscr{P}$ are the total kinetic and potential energies, respectively. The kinetic energy is defined as

$$\mathscr{K} = \langle([(u^2 + w^2)/2]\rangle_{xz}, \tag{7.2}$$

and the potential energy is

$$\mathscr{P} = \frac{Ri_0}{R}\langle z\rho\,(z)\rangle_{xz}, \tag{7.3}$$

where R is the ratio of the characteristic scale of velocity variation to that of the density variation and $\langle\,\rangle_i$ represents averaging over co-ordinate i. The rate of change of the kinetic energy can be written as

$$\frac{\mathrm{d}\mathscr{K}}{\mathrm{d}t} = -\frac{Ri_0}{R}\langle\rho w\rangle_{xz} - \frac{1}{Re}\langle(\nabla\boldsymbol{u})^2\rangle_{xz} \tag{7.4}$$

$$= -\mathscr{H} + \mathscr{D}, \tag{7.5}$$

where $\mathscr{H}$ is the buoyancy flux, and $\mathscr{D}$ is a negative-definite term which represents the loss of kinetic energy of the system to internal energy through viscous dissipation. The time rate of change of the potential energy can be written as

$$\frac{\mathrm{d}\mathscr{P}}{\mathrm{d}t} = \mathscr{H} + \mathscr{D}_p, \tag{7.6}$$

where $\mathscr{D}_p$, a strictly positive quantity, is the rate at which the potential energy of a statically stable and motionless density stratification would increase through conversion of internal energy to potential energy. It can be calculated from the expression

$$\mathscr{D}_p = \frac{Ri_0(\rho_{bottom} - \rho_{top})}{hRePr}, \tag{7.7}$$

where ρ_{bottom} and ρ_{top} are the non-dimensionalized densities at the top and bottom boundaries and h is the vertical extent of the flow domain (30 non-dimensional units in our simulations). Equation (7.5) demonstrates that the total kinetic energy of the system can be decreased through a positive $\mathcal{H}$, which corresponds to a relative net upward motion of dense fluid. This leads to an increase in the potential energy of the system as expressed by (7.6). The reverse follows for a negative $\mathcal{H}$. Apart from the transfer of energy between the kinetic and potential energy reservoirs through the buoyancy flux, total energy can be lost to internal energy by two mechanisms, namely: loss of kinetic energy through viscous dissipation ($\mathcal{D}$) and loss of potential energy through $\mathcal{D}_p$. In other words, combining (7.1), (7.5) and (7.6) gives

$$\frac{\mathrm{d}E}{\mathrm{d}t} = \mathcal{D} + \mathcal{D}_p, \tag{7.8}$$

where the right-hand side is negative definite and $|\mathcal{D}| \gg |\mathcal{D}_p|$.

The potential energy itself can be divided into two parts namely the background potential energy, $\mathcal{P}_B$, defined as

$$\mathcal{P}_B = \frac{Ri_0}{R} \langle z\rho_B(z) \rangle_z, \tag{7.9}$$

and the available potential energy, $\mathcal{P}_A$. So, we have

$$\mathcal{P} = \mathcal{P}_B + \mathcal{P}_A. \tag{7.10}$$

The background density profile $\rho_B(z)$ is the profile associated with the minimum potential energy that the system can obtain if allowed to come to rest in an adiabatic fashion. The resulting profile is a stable density profile which decreases monotonically upward (Winters *et al.* 1995; Caulfield & Peltier 2000). Here $\mathcal{P}_B$ can only be increased through irreversible mixing processes denoted by $\mathcal{M}$ and through $\mathcal{D}_p$ as

$$\frac{\mathrm{d}\mathcal{P}_B}{\mathrm{d}t} = \mathcal{M} + \mathcal{D}_p. \tag{7.11}$$

Combining this with (7.6) and (7.10) we may therefore write

$$\frac{\mathrm{d}\mathcal{P}_A}{\mathrm{d}t} = \mathcal{H} - \mathcal{M} = \mathcal{S}. \tag{7.12}$$

The available potential energy is that part of the total potential energy which is 'available' to be converted back to kinetic energy. Hence, the right-hand side of (7.12), $\mathcal{S}$, simply represents the reversible stirring of the flow whereas the right-hand side of (7.11) represents irreversible mixing. Using the definitions of mixing and stirring, and by combining (7.5) and (7.12) we may therefore write

$$\frac{\mathrm{d}\mathcal{K}}{\mathrm{d}t} = -\mathcal{S} - \mathcal{M} + \mathcal{D}, \tag{7.13}$$

which provides a more transparent interpretation of (7.5): the kinetic energy can be changed through stirring of the fluid, irreversible mixing of the fluid, or viscous dissipation. We note that the right- and left-hand sides of (7.5) can be independently calculated from the density and velocity fields at each instant of the flow evolution. Hence, the agreement between the left- and right-hand sides acts as an independent measure of the accuracy of our simulations. For all of the cases considered in this work, this criterion was satisfied to one part in 10^4 (after non-dimensionalizing both sides of (7.5) by dividing them by $\mathcal{K}$).

The first term on the right-hand side of (7.13) represents a reversible process whereas the two last terms represent irreversible processes. Hence, an instantaneous mixing efficiency can be defined as the ratio of the rate at which kinetic energy is lost to mixing, and the rate at which it is lost to both mixing and dissipation:

$$\mathscr{E}_i = \frac{\mathscr{M}}{\mathscr{M} - \mathscr{D}}. \tag{7.14}$$

By definition, $\mathscr{E}_i$ is smaller than one. Similar to Caulfield & Peltier (2000), the cumulative mixing efficiency (a quantity which can be used for comparison to experiments) is defined as

$$\mathscr{E}_c = \frac{\displaystyle\int_0^t \mathscr{M}(t')\, \mathrm{d}t'}{\displaystyle\int_0^t \mathscr{M}(t')\, \mathrm{d}t' - \int_0^t \mathscr{D}(t')\, \mathrm{d}t'}. \tag{7.15}$$

Figure 13(*a*) shows plots of the time variations of the total kinetic energy of the system for the cases considered in this study plus $c1$-1000-0.12 from *MP1*. Figure 13(*b*) shows the evolution of the corresponding kinetic energy of the primary KH wave for each case. The corresponding potential energies for each case are also shown in figure 18. During the early stages of flow evolution, the total kinetic energy of the system decreases rapidly due to the roll-up of the KH billow. The kinetic energy lost is stored in the cores in the form of potential energy due to the net upward motion of heavy fluid (a positive buoyancy flux). Even though the total kinetic energy decreases with time, the kinetic energy associated with the KH wave itself, $\mathscr{K}_{KH}$ (for the formula (4.16-*MP1*)), grows during this period. So, the KH billow extracts its energy from the background flow. Once the billows saturate, the variations in $\mathscr{P}$, $\mathscr{K}$ and $\mathscr{K}_{KH}$ become small up until the onset of the pairing process. Once the pairing gets underway, a second sharp decrease in $\mathscr{K}$ occurs which again amounts to an increase in the potential energy and also in $\mathscr{K}_{KH}$. Comparing the $Re = 2000$ curves in figure 13(*a,b*) shows that as the Richardson number increases from 0.04 to 0.12, the decrease in $\mathscr{K}$ (and, hence, the increase in $\mathscr{K}_{KH}$) becomes more extreme. This is because in this range, the billow amplitude does not change significantly with Ri_0 and therefore more energy is required to lift the heavier fluid (at higher Ri_0) upward. From $Ri_0 = 0.12$ to 0.16 and 0.2, however, the decrease in $\mathscr{K}$ (and the increase in $\mathscr{K}_{KH}$) becomes smaller due to the significant reduction in the KH billow amplitude at high levels of stratification which amounts to less net upward displacement of heavy fluid. Since the maximum billow amplitude is primarily a function of Ri_0, the evolution of the cases $c1$-1000-0.12 and $c1$-2000-0.12 are similar at early stages and up to the point when secondary vortices form on the braid in $c1$-2000-0.12. This can be verified by comparing the $\mathscr{K}$ curves corresponding to the two cases (thick and thin solid lines in figure 13*a*).

As shown in figure 5 for $c1$-2000-0.12, at $90 < t < 100$ the braid deforms at its centre and two vortices form upon it. The thick solid curve in figure 13(*a*) shows that this coincides with an increase in the total kinetic energy. Figure 18(*c*) also shows that this is coincident with a decrease in the potential energy (which can be verified by comparing the solid and thin lines). So, even though the primary KH billow extracts its energy from the kinetic energy of the shear layer, the secondary instabilities growing on the braid extract their energy from the potential energy stored in the KH billow.
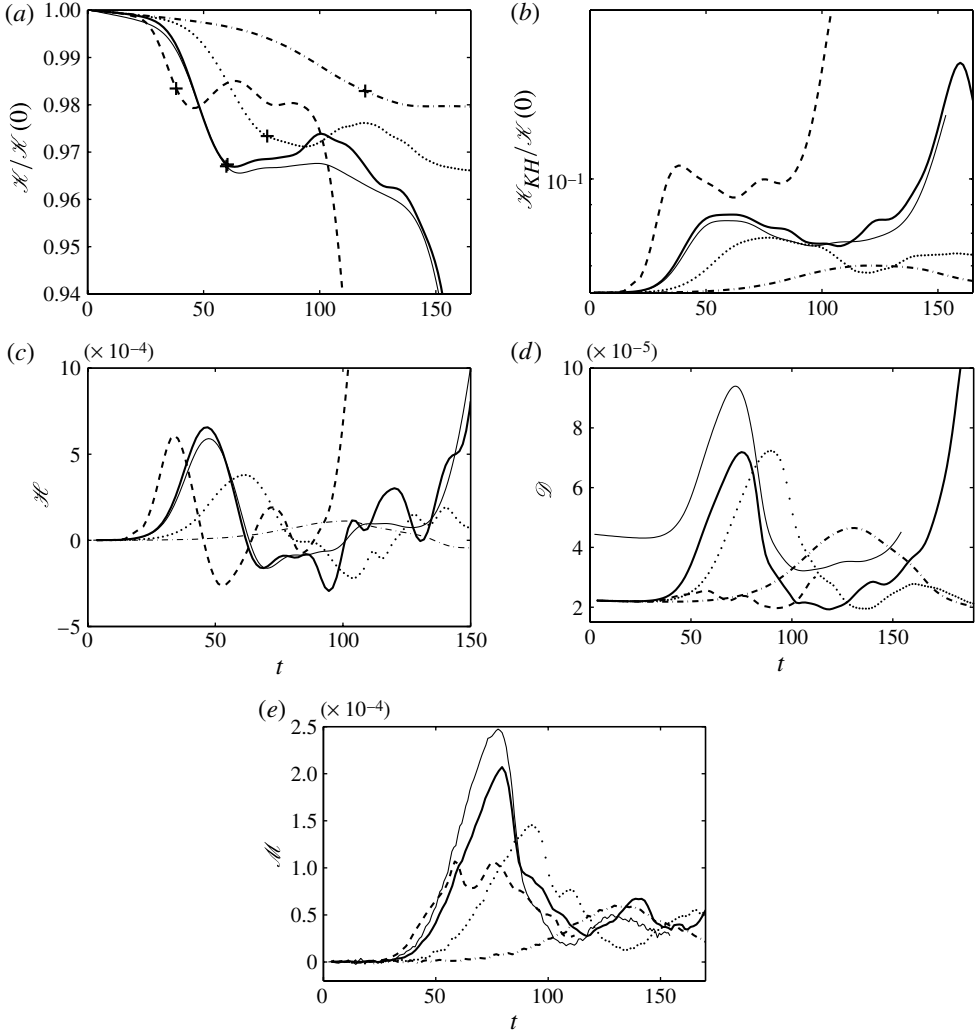
FIGURE 13. (*a*) Total kinetic energy, $\mathcal{K}$, normalized by its value at time $t = 0$, $\mathcal{K}(0)$. (*b*) Kinetic energy of the two-dimensional disturbances (the evolving KH billow) normalized by $\mathcal{K}(0)$. (*c*) Buoyancy flux $\mathcal{H}$. (*d*) Dissipation rate $\mathcal{D}$. (*e*) Irreversible mixing $\mathcal{M}$ plotted for the four cases considered in this study plus the case from *MP1*. Line attributes are: dashed thick solid line for $c1$-2000-0.04; thick solid line for $c1$-2000-0.12; dotted line for $c1$-2000-0.16; thick dashed-dotted line for $c1$-2000-0.2; and thin solid line for $c1$-1000-0.12.

Figure 13(*c*) shows the time variations of the buoyancy flux, $\mathcal{H}$, which quantifies the exchange between the kinetic and potential energy reservoirs and is an important parameter in the parametrization of mixing in large-scale climate models of the oceans and atmosphere. As the Richardson number increases from small values to moderate values (e.g. from 0.04 to 0.12), the maximum amplitude of the KH billow does not change significantly and the peak in $\mathcal{H}$ increases slightly with stratification. However, as Ri_0 tends towards large values (e.g. 0.16 and 0.2), the maximum wave amplitude decreases considerably leading to a decrease in the maximum buoyancy flux. For all cases, $\mathcal{H}$ peaks at the time of saturation of the KH billow and for time periods
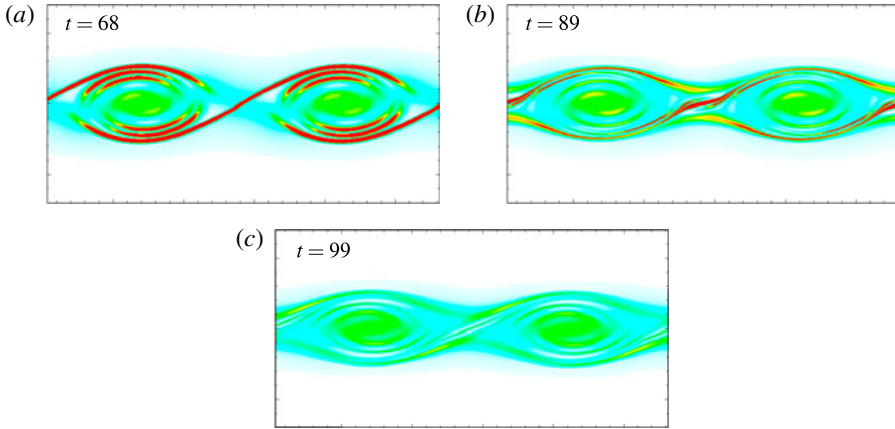
FIGURE 14. Contours of the local dissipation rate, computed for various times for the case $c1$-1000-0.12 considered in *MP1*. Contour levels range from 3.75×10^{-4} for dark red to 0.75×10^{-4} for dark blue.
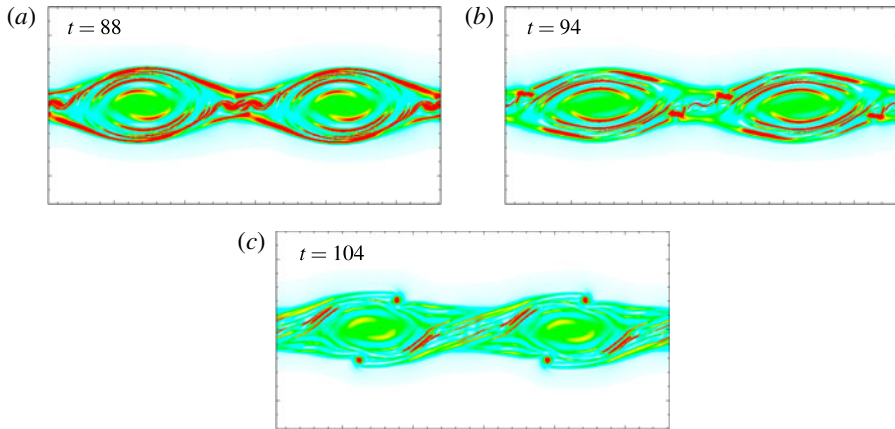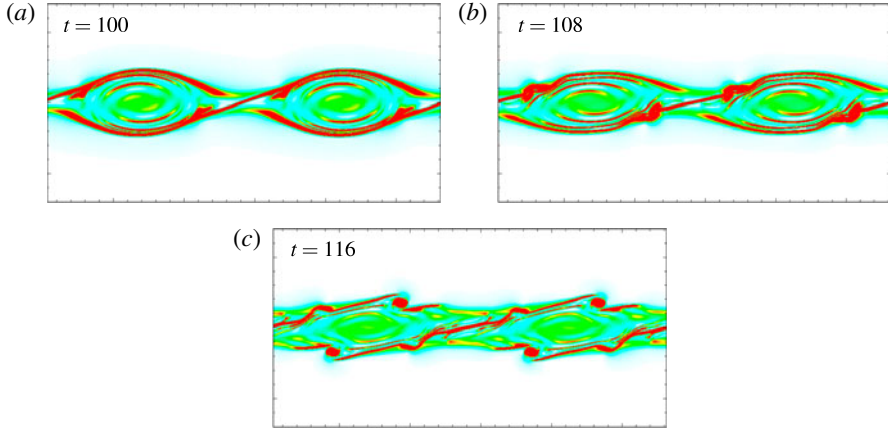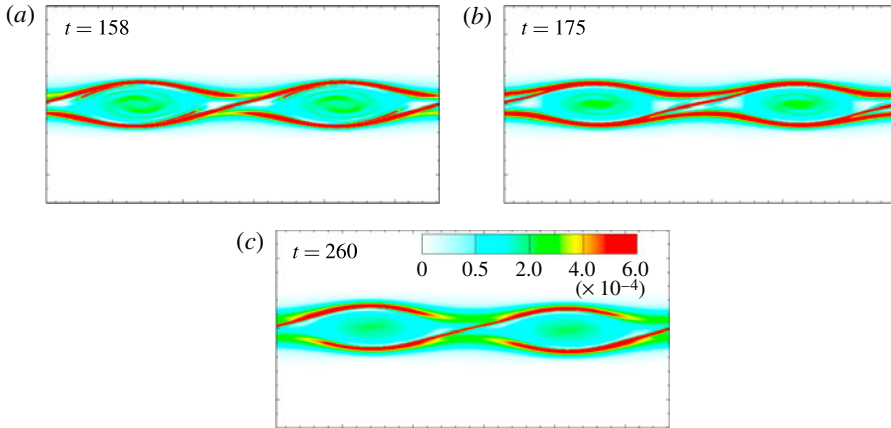

FIGURE 15. Same as figure 14 but for the case $c1$-2000-0.12.

beyond t^*, it decreases, becomes negative and then oscillates about zero before a second rise occurs due to vortex pairing.

Figure 13(d) records the time variations in the total rate of kinetic energy dissipation, $\mathcal{D}$. To help in understanding these time variations, we have plotted colour maps of the dissipation rate for our simulations in figures 14–17. We interpret figures 13(d) and 14–17 together. In general, the preturbulent dissipation rate is considerably smaller than that after the transition to turbulence. On the other hand, the irreversible mixing is still relatively high in the preturbulent phase due to roll-up of layers of light and heavy fluid. Thus, in the denominator of (7.14), $\mathcal{D}$ is smaller than $\mathcal{M}$ in the preturbulent phase leading to large values (~ 1) for the mixing efficiency.

Figure 13(d) shows that the maximum amount of dissipation occurs after the KH billows saturate and before the onset of the pairing process. The rapid increases in the dissipation curves are due to the fast roll-up of the KH wave. The decreases in

FIGURE 16. Same as figure 14 but for the case c1-2000-0.16.

FIGURE 17. Same as figure 14 but for the case c1-2000-0.2.

the dissipation rate curves are due to fast draining of the vorticity from the braid which is characteristic of the onset of the pairing instability. This can be seen in figures 14(c), 15(c) and 17(c). The second rise in the curves of figure 13(d) are due to vortex pairing which leads to formation of a new braid and roll-up of the adjacent cores into a single core. Comparing the solid thick and solid thin lines in figure 13(d), which correspond to cases c1-2000-0.12 and c1-1000-0.12, respectively, shows that the lower-Reynolds-number case has a considerably larger dissipation rate. Since in both simulations the background velocity and density profiles are identical, a higher Reynolds number should be interpreted as implying a higher momentum diffusivity. Therefore, it is expected that the more viscous case (i.e. the lower Re case) will have larger dissipation. Apart from the difference in magnitude between the two curves, the c1-2000-0.12 curve shows a small enhancement in the dissipation rate for $t > 80$. This is due to the braid deformation and formation of secondary vortices on the braid as shown in figure 15. A similar behaviour is observed for case c1-2000-0.16 as shown by the dotted curve in figure 13(d) and by the dissipation contours in

figure 16. Investigating the effect of stratification on dissipation by comparing the $Re = 2000$ cases in figure 13(d), we find that $\mathscr{D}$ is a non-monotonic function of Ri_0. The dissipation rate increases (by nearly one order of magnitude) from the case with $Ri_0 = 0.04$ to cases with $Ri_0 = 0.12, 0.16$. This is due to the increase in the baroclinicity which leads to larger shear in the braid and in the vorticity bands in the cores. The dissipation rate decreases as $Ri_0 \rightarrow 0.2$ due to the decrease in the amplitude of the KH billow which leads to both a smaller number of vorticity bands forming inside the core and a smaller braid tilt angle (which acts so as to reduce the baroclinic production of vorticity). This can be seen by comparing figures 15, 16 and 17.

Figure 13(e) shows time variations in the irreversible mixing, $\mathscr{M}$, with respect to time. Similar to the dissipation rate, $\mathscr{M}$ peaks after the billows saturate. This irreversible mixing in the preturbulent phase is associated with the statically unstable regions induced within the billows. So, the contribution of the braid to this should be negligible. However, comparison between the solid thick and solid thin lines (corresponding to $c1$-2000-0.12 and $c1$-1000-0.12, respectively) reveals an increase in the mixing for the $Re = 2000$ case for $t > 80$. This occurs for two reasons. First, the braid deformation induces further irreversible mixing by forming small-scale structures on the braid as can be seen in figure 15. A second and more important reason is that once the secondary vortices form on the braid, they propagate around the periphery of the cores distorting their internal structures and by so doing further enhance the irreversible mixing. This can be seen in figures 15 and 16. The $Ri_0 = 0.16$ curve in figure 13(e) shows a significant enhancement in $\mathscr{M}$ in the form of a second peak at $t \sim 108$ which is the time when secondary vortices form at the corners of the braid (see the $t = 108$ frame in figure 16). Comparing the $Re = 2000$ cases in figure 13(e) shows a weaker but similar dependence on Ri_0 to that in figure 13(d) which occurs for the reasons explained above.

Figure 18(a,c,e,g) show plots of the potential energies and figure 18(b,d,f,h) show the mixing efficiencies for our four cases. According to (7.6), (7.11) and (7.12), $\mathscr{P} - \mathscr{D}_p t - \mathscr{P}(0)$, $\mathscr{P}_B - \mathscr{D}_p t - \mathscr{P}_B(0)$ and $\mathscr{P}_A(t) - \mathscr{P}_A(0)$ are merely time integrals of $\mathscr{H}$, $\mathscr{M}$ and $\mathscr{S}$, respectively. At early stages of the billow roll-up, most of the increase in the potential energy is due to stirring. Thus, the available and total potential energy curves almost coincide. The increase in the available potential energy is a reversible process and some of this energy is returned to the kinetic energy reservoir. This is shown by the slight rise followed by a rapid fall in $\mathscr{H}$ in figure 13(a). This reverse transfer of energy is imperfect, however, and part of the available potential energy is lost to irreversible mixing and a corresponding increase in the background potential energy. So, as the gap between the available and total potential energies grows larger, so does $\mathscr{P}_B$. Comparing the $c1$-2000-0.12 and $c1$-1000-0.12 cases in figure 18(c) shows a dip in $\mathscr{P}$ for the $Re = 2000$ case at $t \sim 90$ due to the braid instabilities. At approximately the same time, a rise is observed in the $\mathscr{P}_A$ curve of the $Re = 2000$ case which is due to the stirring induced by the braid deformation and the roll-up of secondary vortices on the braid.

Figure 18(b,d,f,h) show instantaneous and cumulative mixing efficiencies. The curves are cut prior to the onset of significant growth of the pairing instability to focus on the preturbulent mixing phase only (based on our stability analysis, we assume that by the time of onset of the pairing instability, the SCI would already have influenced the onset of turbulent collapse). As expected, $\mathscr{E}_i$ possesses values near unity due to small dissipation rates. The oscillations subsequent to the initial peaks in $\mathscr{E}_i$ are due to re-creation of statically unstable regions inside the cores as the KH billows continue to roll up. Comparing the cumulative mixing efficiency curves for the four $Re = 2000$
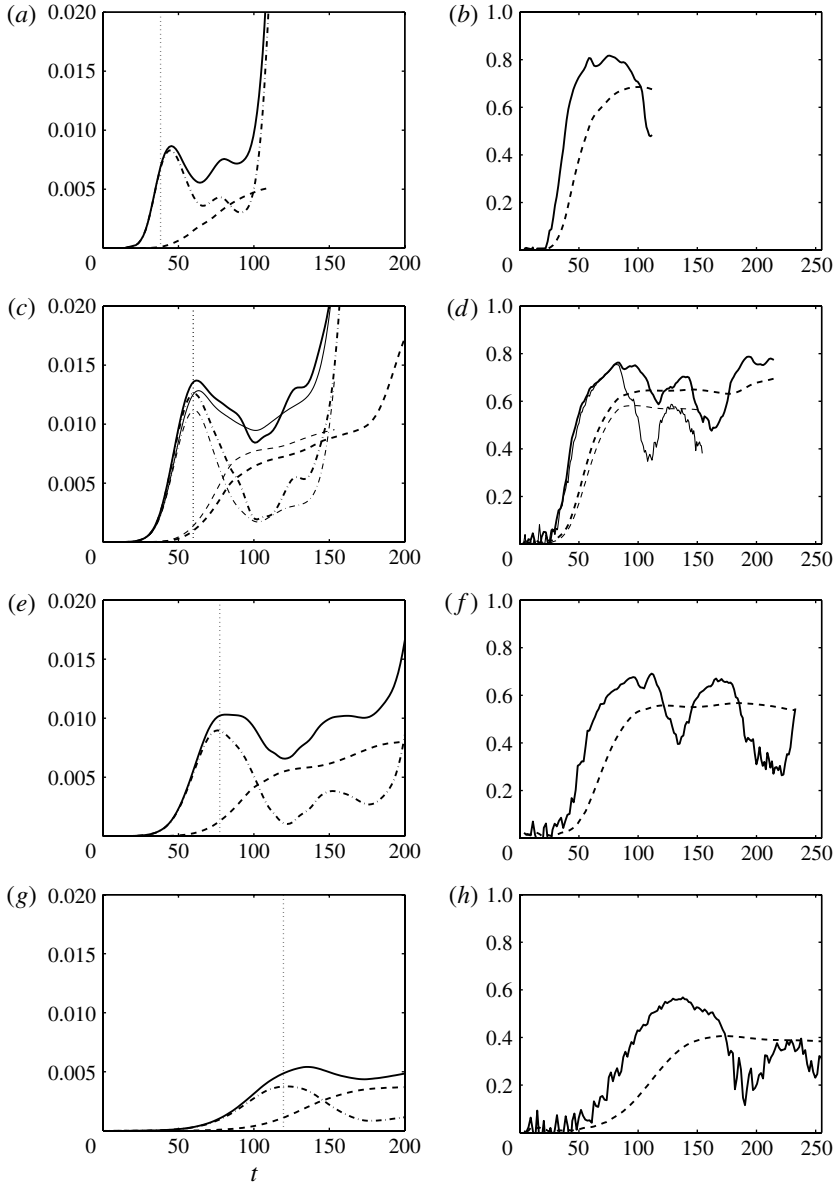
FIGURE 18. (*a,c,e,g*) Time variation of $\mathscr{P} - \mathscr{D}_p t - \mathscr{P}(0)$ (solid line), $\mathscr{P}_A(t) - \mathscr{P}_A(0)$ (dash-dotted line) and $\mathscr{P}_B - \mathscr{D}_p t - \mathscr{P}_B(0)$ and (*b,d,f,h*) time variation of the instantaneous mixing efficiency $\mathscr{E}_i$ (solid line) and cumulative mixing efficiency $\mathscr{E}_c$ (dashed line). Cases: (*a,b*) $c1$-2000-0.04; (*c,d*) $c1$-2000-0.12 and $c1$-1000-0.12; (*e,f*) $c1$-2000-0.16; (*g,h*) $c1$-2000-0.2. In (*c,d*), the thick lines correspond to case $c1$-2000-0.12 while the thin lines correspond to $c1$-1000-0.12. The vertical dotted lines in (*a,c,e,g*) show the climax time t^* for each case.

cases, we find that the efficiency of mixing decreases monotonically with increase in Ri_0. It was shown in Caulfield & Peltier (2000) that $\mathscr{E}_c$ increases (slightly) with Ri_0 for $0.025 < Ri_0 < 0.1$. Our results, however, demonstrate that $\mathscr{E}_i$ decreases as Ri_0 is further increased beyond 0.1 and tends to 0.2. To explain the increase and decrease
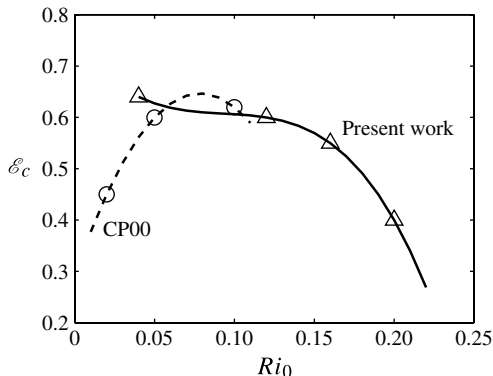
FIGURE 19. Cumulative mixing efficiencies for the preturbulent phase obtained by combining the results of our work with those of figure 5 of Caulfield & Peltier (2000).

in $\mathscr{E}_c$ with Ri_0, we consider figure 13(d,e) simultaneously. For very small Ri_0, the dissipation rate is very low and, hence, $\mathscr{E}$ is large. As Ri_0 increases from 0.04 to 0.12, $\mathscr{D}$ increases and so does $\mathscr{M}$. The net effect is a very slight decrease in the cumulative efficiency (for $Re = 750$ the net effect is a very slight increase as shown in Caulfield & Peltier (2000)). As Ri_0 is increased from 0.12 to 0.2, the irreversible mixing $\mathscr{M}$ decreases substantially (due to the smaller core amplitudes) while the dissipation rate does not decrease as significantly as $\mathscr{M}$. Hence, the net effect is a decrease in $\mathscr{E}_c$ from $\sim$0.65 for $Ri_0 = 0.12$ to $\sim$0.4 for $Ri_0 = 0.2$. Figure 19 shows the plot of the preturbulent cumulative mixing efficiency versus Ri_0 obtained by combining our results with those of Caulfield & Peltier (2000). Even though our results were obtained for cases with $Re = 2000$ whereas (Caulfield & Peltier 2000) cases were for $Re = 750$, preturbulent $\mathscr{E}_c$ does not seem to be particularly sensitive to Reynolds number for the range common to the two studies ($0.04 < Ri_0 < 0.1$) and it is a much stronger function of the Richardson number. Figure 19 clearly shows the non-monotonic variations in preturbulent $\mathscr{E}_c$ with the stratification. It is important to note that we have limited the range of time for our time series of mixing efficiency to the time period prior to the emergence of transition-inducing three-dimensional instabilities.

8. Discussion

We have herein extended the analyses presented in *MP1* by performing secondary stability analysis for a sequence of density stratified unstable shear layers at higher Reynolds number and for a range of Richardson numbers. As one of the important findings of this work we showed that the growth rate of SSI of the braid is increasingly suppressed as a function of time by the growth of the background KH vortex cores due to the evolution of the strain field. The degree of this suppression is an increasing function of the stratification level, becoming larger for larger values of Ri_0. The infinite-length-of-the-braid assumption of Corcos & Sherman (1976) is only valid at earliest stages of flow evolution when the cores remain compact. We have shown that secondary vortex formation on the braid may be triggered by the growth of another secondary instability (such as the LCVI or SVBI). The wavelength and growth rate of the vortices formed on the braid in this fashion can be affected by precursor instabilities. It is very important to note that these braid secondary vortices are not of SSI type.

Further new modes of secondary instability were also revealed by the analyses described in this paper. One of these, which we have labelled SCDI, tends to inflate the vortex cores on the diagonal (almost parallel to the braid). This mode is of a three-dimensional nature with small wavenumbers and weakens at high Richardson numbers. No evidence of the growth of this mode was observed in our simulations for the two-dimensional background flows that were subjected to secondary stability analyses. A second new three-dimensional instability discovered in this work was the LCVI, which corresponds to formation of vortices at the tips of the fully developed vorticity bands within the cores. This instability exists over a very large range of spanwise wavenumbers (the entire range considered in this study which is from 0 to 12 in non-dimensional units) and its growth rate increases with increase in either the Reynolds or Richardson numbers. Finite-amplitude growth of this mode was observed in our two-dimensional simulations. Of greater importance than either of these new modes is most probably the SPI discussed in *MP1*, which has herein been shown to exist over the broad range of stratification levels considered. In all cases, SPI has been shown to develop high growth rates at large wavenumbers comparable to those of the SCI. SPI (along with SCI) may well play a critical role in inhibiting the occurrence of the pairing interaction at high Reynolds numbers (associated with geophysical flows) which is fundamental to the support of an upscale cascade of energy in stratified turbulence via this mechanism (see e.g. Peltier & Stuhne (2002) for a general discussion). Although the SPI mode has a two-dimensional counterpart it is much stronger in three dimensions. The pairing instability itself was found to be characterized by only weak sensitivity to the stratification (compared with other secondary modes). As this mode exists from very early stages of flow evolution, and as it maintains its growth rate for a long period of time, it ultimately leads to vortex pairing in two-dimensional simulations. In a fully three-dimensional flow, however, we expect the interaction of one or more of the instabilities we have found to mark a rapid transition to turbulence will serve to inhibit the occurrence of vortex pairing.

Our analyses have also shown that increase in the Reynolds number leads to increase in the growth rate of all of the secondary instabilities found by our stability analysis. An increase in the Richardson number from small to moderate values (0.04–0.12 in our study) leads to an increase in the growth rate of the secondary instabilities while further increase in the Richardson number from moderate to high (0.12–0.2 in our study) stratification levels leads to decrease in the growth rate due to the stabilizing effects of the stratification. In general, most of the findings of our analyses in this paper are in agreement with the predictions of the heuristic model of *MP1*.

Our analyses of the energetics of the flow demonstrated that while the primary KH wave absorbs its energy from the background kinetic energy reservoir, the secondary instabilities absorb their energy from the available potential energy reservoir. Buoyancy flux, viscous dissipation, and irreversible mixing associated with the preturbulent KH wave were all characterized by an increase–decrease behaviour with increase in the stratification level. It was shown that even though the viscous dissipation is not greatly sensitive to stratification level in the preturbulent phase, the irreversible mixing does increase considerably with Ri_0. Our analyses revealed that emergence of braid instabilities leads to a slight increase in the viscous dissipation as well as to a larger increase in the irreversible mixing thereby increasing the preturbulent mixing efficiency. Our results (for $0.02 < Ri_0 < 0.1$) together with those of Caulfield & Peltier (2000) (for $0.02 < Ri_0 < 0.2$) show an increase in the cumulative mixing efficiency

with increase in Ri_0 from small to moderate levels, and a decrease in the efficiency with further increase of Ri_0 from moderate to high stratification levels.

Even though the range of Reynolds number considered in our stability analyses was low compared with geophysical flows, it was sufficiently high to reveal the existence and characteristics of various new and important secondary modes which have been reported in recent observations (see Geyer *et al.* (2010) for evidence of a train of secondary shear vortices on the braid, similar to the eigenfunction of SSI reported in our work; see Moum *et al.* (2003) for a possible example of SPI forming in a KH billow growing on the interface of an internal solitary wave approaching the shore). Moreover, our stability analyses validated the predictions of the heuristic model of *MP1* (which extend to $Re = 10^4$ and $Pr = 7$) for $Re < 2000$ and $Pr = 1$. Therefore, that model can provide insight into a new interpretation of geophysical flows which was not possible based on laboratory experiments of stratified shear layers (due to their limited range of flow parameters). Based on the work in *MP1* and this paper, we conclude that the SCI will remain a key three-dimensional instability in transition to turbulence at high Reynolds ($O(10^4)$) and Prandtl numbers in the range 1–8. This regime is relevant for both the heat stratified oceanic and atmospheric shear layers. Moreover, SSI of the braid is expected to grow at early stages of flow evolution at Reynolds numbers beyond a critical value (which depends on both Pr and Ri_0). Below this level, isolated shear vortices (not an SSI wave train) may still roll up on the braid due to deformations induced by other local instabilities which grow on the braid (such as SPI, SVBI) or which grow inside the cores (such as the LCVI). The likelihood of occurrence of SSI diminishes at very small stratification levels. Moreover, at a fixed Re and Ri_0, increase in Pr suppresses the SSI. It will be interesting to investigate whether it will be possible for the extended braid shear instability (which was revealed by our analyses and shown in figure 16-*MP1*) to emerge so early and so vigorously at early stages of flow evolution at sufficiently high Reynolds numbers to distort the internal core structure and inhibit occurrence of the core convective instability.

The SPI, which was analysed in detail for the first time in *MP1*, might also emerge in subranges of the Ri_0–Pr–Re space in which SSI and SCI do not destroy the braid structure required for emergence of the SPI. Further investigation is needed to determine the parameter range over which SPI has a chance of emerging, but according to our analyses in *MP1*, $\gamma_s/\Omega < 0.1$ seems to be a qualitatively valid criterion.

Even though vortex pairing seems to be inevitable in two-dimensional simulations of KH waves, we suspect that the 'zoo' of secondary instabilities discussed in *MP1* and in this paper, some of the inhabitants of which are highly three dimensional, will have the potential to facilitate a rapid turbulence transition at high Reynolds numbers and thereby to inhibit vortex pairing. This, in addition to the suppressing influence of stratification on vortex pairing (as discussed in this paper), need to be fully investigated using three-dimensional simulations to identify the regions in parameter space in which pairing is possible and regions in which it is suppressed. Such simulations are also required to study the nonlinear interactions among the inhabitants of the 'zoo' of instabilities identified herein as well as their implications for turbulence transition and mixing efficiency.

Acknowledgements

REFERENCES

CAULFIELD, C. & PELTIER, W. R. 2000 Anatomy of the mixing transition in homogeneous and stratified free shear layers. *J. Fluid Mech.* **413**, 1–47.

CORCOS, G. & SHERMAN, F. 1976 Vorticity concentration and the dynamics of unstable free shear layers. *J. Fluid Mech.* **73**, 241–264.

GARGETT, A. E. & MOUM, J. 1995 Mixing efficiencies in turbulent tidal fronts: results from direct and indirect measurements of density flux. *J. Phys. Oceanogr.* **25**, 2583–2608.

GEYER, W. R., LAVERY, A. C., SCULLY, M. E. & TROWBRIDGE, J. H. 2010 Mixing by shear instability at high Reynolds number. *Geophys. Res. Lett.* **37**, L22607.

KLAASSEN, G. P. & PELTIER, W. R. 1985 The onset of turbulence in finite amplitude Kelvin–Helmholtz billows. *J. Fluid Mech.* **155**, 1–35.

LORENZ, E. N. 1955 Available potential energy and the maintenance of the general circulation. *Tellus* **7**, 157–167.

MASHAYEK, A. & PELTIER, W. R. 2012 The 'zoo' of secondary instabilities precursory to stratified shear flow transition. Part 1 Shear aligned convection, pairing, and braid instabilities. *J. Fluid Mech.* **708**, 5–44.

MOUM, J. N. 1996 Efficiency of mixing in the main thermocline. *J. Geophys. Res.* **101**, 12057–12069.

MOUM, J. N., FARMER, D. M., SMITH, W. D., ARMI, L. & VAGLE, S. 2003 Structure and generation of turbulence at interfaces strained by internal solitary waves propagating shoreward over the continental shelf. *J. Phys. Oceanogr.* **33**, 2093–2112.

PELTIER, W. R. & CAULFIELD, C. 2003 Mixing efficiency in stratified shear flows. *Annu. Rev. Fluid Mech.* **35**, 135–167.

PELTIER, W. R. & STUHNE, G. R. 2002 The upscale turbulent cascade: shear layers, cyclones and gas giant bands. In *Meteorology at the Millennium* (ed. R. P. Pierce). Academic.

RUDDICK, B. T., WALSH, D. & OAKEY, N. 1997 Variations in apparent mixing efficiency in the north atlantic central water. *J. Phys. Oceanogr.* **27**, 2589–2605.

SMYTH, W. D. 2003 Secondary Kelvin–Helmholtz instability in weakly stratified shear flow. *J. Fluid Mech.* **497**, 67–98.

SMYTH, W. D. & MOUM, J. N. 2000 Length scales of turbulence in stably stratified mixing layers. *Phys. Fluids* **12**, 1327–1342.

SMYTH, W. D., MOUM, J. & CALDWELL, D. 2001 The efficiency of mixing in turbulent patches: inferences from direct simulations and microstructure observations. *J. Phys. Oceanogr.* **31**, 1969–1992.

STAQUET, C. 2000 Mixing in a stably stratified shear layer: two- and three-dimensional numerical experiments. *Fluid. Dyn. Res.* **27**, 367–404.

WINTERS, K., LOMBARD, P., RILEY, J. & D'ASARO, E. A. 1995 Available potential energy and mixing in density-stratified fluids. *J. Fluid Mech.* **289**, 115–128.